CHEMISTRY OF MATERIALS
Cite This: Chem. Mater. 2019, 31, 862−872
Article
pubs.acs.org/cm

Enhanced Thermoelectric Performance of Yb-Single-Filled Skutterudite by Ultralow Thermal Conductivity

Wenjie Li,*[,†,⊥] Jue Wang,[§] Yuantao Xie,[∥] Jennifer L. Gray,[‡] Jean J. Heremans,[∥] Han Byul Kang,[⊥] Bed Poudel,[†,⊥] Scott T. Huxtable,[§] and Shashank Priya*[,†,⊥]

[†]Department of Materials Science and Engineering and [‡]Materials Research Institute, The Pennsylvania State University, University Park, Pennsylvania 16802, United States

[§]Department of Mechanical Engineering, [∥]Department of Physics, and [⊥]Center for Energy Harvesting Materials and Systems (CEHMS), Virginia Tech, Blacksburg, Virginia 24061, United States

Supporting Information

ABSTRACT: The filling fraction limitation (FFL) in n-type $CoSb_3$ skutterudites is far below that of p-type $(Fe,Co)Sb_3$-based skutterudites, and it is critical to increase FFL for accomplishing high thermoelectric figure of merit (ZT_{max}). Here, a series of $Yb_xCo_{4-y}Fe_ySb_{12}$ alloys with x = 0.25−0.5 and y = 0.1−0.5 were synthesized, which demonstrate a clear increase of the FFL of Yb from ∼0.3 in $CoSb_3$ to 0.5. Ultralow thermal conductivities of 2.0−2.5 W/m·K at 300 K and 1.75 W/m·K at ∼600 K have been achieved, which are the lowest values reported among skutterudite materials and comparable with p-type skutterudites. These ultralow thermal conductivities result from the combination of secondary phase scattering and phonon scattering from dynamic electron exchange between Fe^{2+} and Co^{3+}. High ZT_{max} values of 1.28 at 740 K and 1.34 at 780 K are obtained, which are among the best values reported in the temperature range of 740−800 K. The temperature at which maximum ZT_{max} appears is shifted below 850 K. These results are highly exciting toward the development of multistage segmented and cascade thermoelectric power generators for in-air operations.

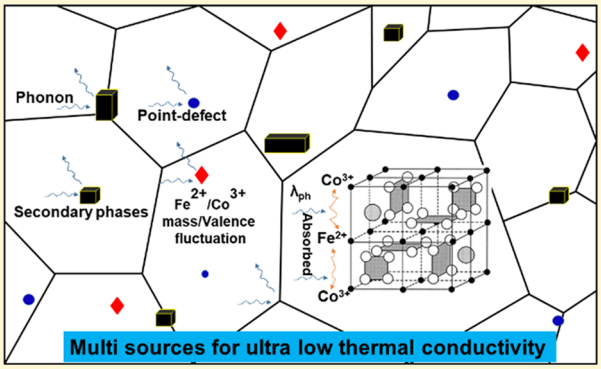

1. INTRODUCTION

Thermoelectric (TE) modules are solid-state devices commonly used for converting waste heat into electricity and for thermal cooling.[1−4] The performance of TE materials is characterized by dimensionless figure of merit, $ZT = S^2\sigma T/\kappa$, where S is the Seebeck coefficient (thermopower), σ is the electrical conductivity, T is the absolute temperature, and κ is the total thermal conductivity. To obtain high ZT, it is crucial to maximize the power factor (PF) $S^2\sigma$ and simultaneously minimize κ. The parameters S, σ, and κ are generally correlated with each other, which prohibits the simultaneous optimization of electrical and thermal transport to achieve higher ZT.

Among various state-of-the-art TE materials, $CoSb_3$ has attracted the greatest interest because of its reasonable band gap, high carrier mobility,[5,6] relatively low cost, and benign constituent elements compared to other TE materials, for example, $CoAs_3$ and PbTe.[7−11] The thermal conductivity of binary $CoSb_3$ is large, resulting in very low ZT and, thus, poor thermal-to-electrical conversion efficiency.[12−15] However, skutterudites filled with various guest atoms[16−23] in the nanocages distinguish themselves as better TE materials exhibiting a phonon glass−electron crystal behavior[24] by simultaneously possessing low thermal conductivity like a glass and high electrical conductivity like a crystal. The fillers loosely bound to Sb host atoms in the intrinsic nanocages result in Einstein-like vibrational modes that can strongly scatter phonons and reduce lattice thermal conductivity ($\kappa_{lattice}$).[25−27] Yb-filled skutterudites show remarkable TE properties around 850 K due to their small ionic radius and heavy atomic mass as compared to other fillers, which leads to low thermal conductivity because of the lowest rattling frequency of ∼42 cm^{-1} in $CoSb_3$.[28,29] It is expected that Yb^{2+} acts as an electron donor, which can alter carrier concentration (n_H) in the range of 10^{19}−10^{21} cm^{-3} to achieve the moderate n_H necessary for the optimization of ZT. Because of the relatively low air and moisture sensitivities of the Yb filler, it is an attractive material for the TE generator (TEG) used in waste heat recovery from automobile exhaust.[30]

Despite extensive studies on Yb-filled skutterudites, the fractional occupancy of voids, or the so-called filling fraction limitation (FFL), has still not been conclusively determined. Many theoretical studies have attempted to calculate the FFL of fillers,[31,32] in addition to many experimental efforts.[29,33−40] These results demonstrate that FFL is very low for n-type

Received: September 19, 2018
Revised: January 14, 2019
Published: January 15, 2019

DOI: 10.1021/acs.chemmater.8b03994
Chem. Mater. 2019, 31, 862−872

$CoSb_3$;[41] for example, Ce, Ba, and Eu fillers are less than 0.2, 0.3, and 0.4 for the Co_3Fe matrix,[42−44] and the Ba + Yb filler remains at about 0.4 for the $Co_{3.6}Fe_{0.4}$ matrix.[45] However, in the case of p-type skutterudites, such as Fe_4Sb_{12} and Fe_3CoSb_{12}, comparatively more fillers can be incorporated,[46−48] generally above 90% due to the charge compensation mechanism, where Fe^{2+} contributes as an electron acceptor leading to the augmentation of more filler atoms capable of occupying nanocages.[41] Therefore, Fe substitution on the Co site, represented as $Co_{4-y}Fe_ySb_{12}$, is potentially an effective approach to increasing the FFL of fillers for n-type skutterudites and thereby reducing the lattice thermal conductivity.[49−52] Additionally, the presence of Fe^{2+} creates a larger effective mass, which can also enhance the Seebeck coefficient.[18,41] Wang et al.[34] performed a systematic study on the FFL of $Yb_xCo_4Sb_{12}$ composites and reported a maximum FFL for $Yb_{0.3}Co_4Sb_{12}$ with ZT of ∼1.5 at 850 K. Chen et al.[36] experimentally derived an Yb FFL of 0.6 within a $Co_{3.5}Fe_{0.5}Sb_{12}$ matrix, but room-temperature ZT was only ∼0.11. Very few studies have been conducted on Fe substitution in n-type skutterudite materials such as $(Ba,Yb)_xCo_{3.63}Fe_{0.37}Sb_{12}$[45,53] and $M_{0.7}Co_{3.75}Fe_{0.25}Sb_{12}$.[54] These studies show either limited filling fraction or relatively high thermal conductivity, as plotted in Figure 6b. Most of the Fe substitution work has focused on p-type skutterudites because of the crossover from n-type to p-type even for Co-rich compositions.[16,42,49,53,55−59] Therefore, it remains an open question as to how Fe substitution can systematically influence the FFL of Yb and influence its TE properties for n-type skutterudites.

Recent TEG research has shown that the efficiency of a single-stage device, for example, bismuth telluride,[60] lead telluride,[61] skutterudite,[62−64] and half-Heusler,[65] is relatively low because different materials possess their optimum ZT only in certain temperature ranges. To fully utilize TEG over a broad temperature range (from 300 to 1000 K) with higher efficiency, multistage devices, as shown in Figure S1, are being developed with enhanced overall efficiency.[61,66−70] These multistage devices include segmented and cascade structures where individual materials are used in their preferred temperature range, where their ZT is maximized and the materials avoid deterioration mainly due to oxidation. For instance, bismuth telluride, skutterudite, lead telluride, and half-Heusler materials are ideally applicable below 473 K, 400−673 K, 623−873 K, and 823−1073 K in air atmosphere, respectively. However, the maximum ZT (ZT_{max}) of current filled skutterudites with excellent performance is still too high at roughly ∼850 K.[17,19,34,71] To be a promising candidate for real TE applications in the temperature range of 300−773 K under vacuum or between 400−623 K in air,[4,30,72,73] it is imperative but very challenging to lower the ZT_{max} temperature, leading to an improvement in average ZT (ZT_{avg}).

In this study, we developed a series of $Yb_xCo_{4-y}Fe_ySb_{12}$ ($0.25 \le x \le 0.5$ and $0.1 \le y \le 0.5$) compositions to investigate the Fe-dependent FFL of Yb and quantified the effect of Fe substitution on the TE properties. The polycrystalline specimens were prepared via an optimum melting-annealing-sintering technique. The results clearly demonstrate that the FFL of Yb is up to 0.4 when $y \le 0.2$ and it is beyond 0.5 when $y \ge 0.3$, which is much higher than previously reported theoretical and experimental results on filled $CoSb_3$,[32−34,39,74] indicating that Fe substitution can effectively increase the FFL of Yb. Ultralow thermal conductivity (∼1.7−2.0 W/m·K) was achieved for various compositions, and this conductivity range is about 25−40% lower than that of filled $CoSb_3$ compounds[33−35,37,39] and comparable with p-type skutterudites. As a result of the optimized power factor and ultralow thermal conductivity, we found a ZT value of 1.28 at 740 K for a nominal composition of $Yb_{0.25}Co_{3.75}Fe_{0.25}Sb_{12}$ and a ZT value of 1.34 at 780 K for a nominal composition of $Yb_{0.4}Co_{3.8}Fe_{0.2}Sb_{12}$. These results also indicate that the ZT_{max} temperature has been successfully shifted below 800 K.

2. RESULTS

2.1. Structure and Yb Filling Fraction Limitation (FFL). The XRD pattern of sintered $Yb_xCo_{4-y}Fe_ySb_{12}$ (x = 0.25−0.5; y = 0.1−0.5) pellets is shown in Figure S2. All of the major diffraction peaks can be indexed to body-center cubic $Im\bar{3}$ space groups of skutterudite $CoSb_3$ phase. However, a trace amount of $FeSb_2$ was observed with increasing Fe content when $y \ge 0.4$. The presence of a small amount of $YbSb_2$ phase can only be detected in two cases: $x \ge 0.4$ and $y \le 0.2$ or $x = 0.5$ and $y \le 0.4$. The appearance of $YbSb_2$ impurity indicates that Yb FFL is less than 0.4 when $y \le 0.2$, which can be verified by calculating the lattice parameters as a function of nominal Yb content, as shown in Figure 1a, saturated at a value of ∼9.06 Å. These results are in agreement with similar findings on filled $CoSb_3$ in the literature.[33−35,37,39] However, the linear increase of the lattice parameter a with an increase of Yb content shows a nonsaturated value when the Fe content is higher than 0.25 (shown as hollow dots and green and blue dash lines in Figure 1a). This suggests that Yb FFL should be higher than 0.5 when $y \ge 0.25$. Figure 1b also illustrates a nearly linear increase of carrier concentration as a function of the Yb-filling fraction, which proves that Yb contributes as electron donor-occupied nanocages. The isotropic atomic displacement parameters (ADPs) of the Yb filler were found to be about one order of magnitude larger than those of the Co/Fe and Sb matrix atoms, which is consistent with the results reported in other single-filled skutterudites.[29] Interestingly, the ADPs of Co/Fe were also found to be generally larger than that of Co in a single-filled $CoSb_3$ matrix,[75] probably leading to lower thermal conductivity with higher disordering.

The compositions of sintered pellets were determined by EDS. Table S2 lists the determined compositions and room-temperature transport properties for selected samples. The Yb content is almost the same as the nominal composition, when x is smaller than 0.3. However, the Yb content is smaller than the nominal composition when x is larger than 0.4 and saturates at an Yb content of ∼0.49, which is consistent with previous skutterudite phase diagram study results.[76−79] Figure 1c shows the microstructure of samples #1−#6 (x = 0.25 and y = 0.1−0.5). The grain size varies from a nanometer range to a few micrometers, mostly ∼2 μm, and there is no significant change in grain size with an increase of Fe content. However, coarser and coarser grain boundaries were observed with the increase of Fe content, as shown by marked regions with red lines in Figure 1c. A similar phenomenon was also observed on all other samples. EDS and elemental mapping confirm that these coarse regions relate to the $FeSb_2$ impurity phase, which may not be detected by XRD because of very low volume fraction when the Fe content is less than 0.4. Figure S3 illustrates the trace amounts of nano- to microsized Yb aggregations in samples #1−#6 even in a single-pure phase shown by XRD. This is probably due to the relatively low

DOI: 10.1021/acs.chemmater.8b03994
Chem. Mater. 2019, 31, 862−872

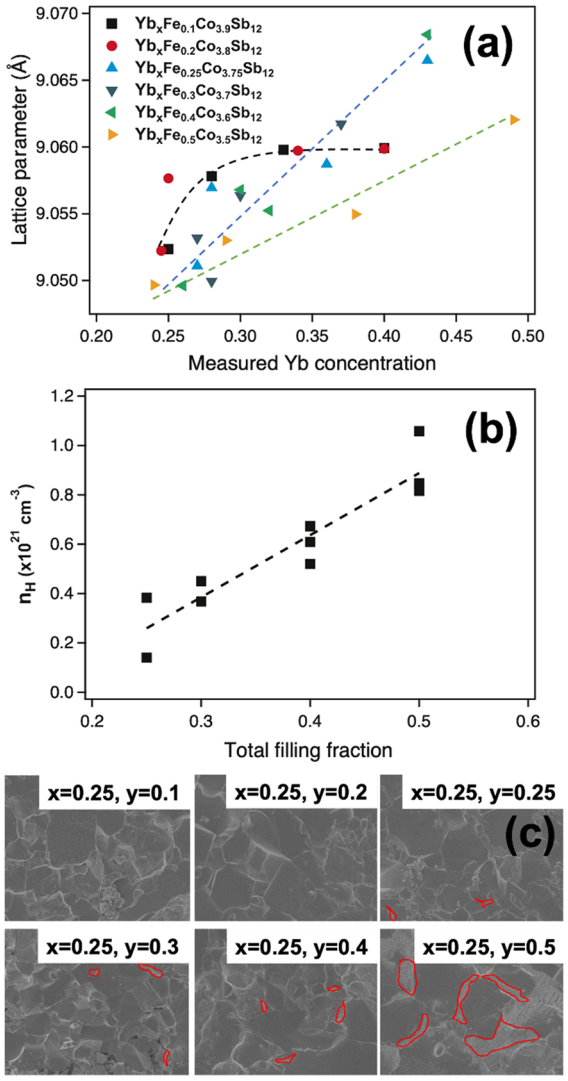

Figure 1. (a) Refined lattice parameter a as a function of nominal Yb content x for $Yb_xCo_{4-y}Fe_ySb_{12}$ sintered pellets, (b) total Yb-filling fraction dependence of carrier concentration, and (c) backscattered electron image of samples #1−#6 (when x = 0.25 and y = 0.1−0.5). The locations are randomly selected in these skutterudite grains for EDX analysis to estimate actual compositions, as shown in Table S2. The marked regions with red lines indicate the coarse grain boundaries where impurity phases form.

quenching rate of the traditional melting-annealing method and its peritectic nature leading to slow kinetics for the formation of the filled skutterudites. The localized secondary phases may change the filling level in a local region and lead to defects along grain boundaries, which could be an effective phonon scattering source. Moreover, because $FeSb_3$ does not exist, microsized $FeSb_2$ aggregations were found in high Fe-content compositions, as shown in Figure S3f. When Yb is beyond saturation, in $Yb_{0.5}Co_{3.8}Fe_{0.2}Sb_{12}$, $Yb_{0.5}Co_{3.75}Fe_{0.25}Sb_{12}$, and $Yb_{0.5}Co_{3.7}Fe_{0.3}Sb_{12}$, for example, it turns to form $YbSb_2$ impurities, as shown in Figure S4. These secondary phases could probably be moderated by applying a novel synthesis method with an ultrahigh cooling rate, for example, melting-spinning.[47]

2.2. Thermoelectric Properties. The selected room-temperature thermoelectric properties, bulk density (ρ), carrier concentration (n_H), and mobility (μ_H) of $Yb_xCo_{4-y}Fe_ySb_{12}$ skutterudites are summarized in Table S2. These results show that, in general, electrical conductivity increases and the absolute value of the Seebeck coefficient decreases with increasing Yb content because Yb^{2+} acts as an electron donor, resulting in higher carrier concentration. It is evident that, as the FFL increases from 0.25 to 0.5, the carrier concentration increases.

Figure 2 shows the temperature dependence of the electrical conductivity (σ), Seebeck coefficient (S), and power factor (PF) for selected samples. The σ, S, and PF properties for all samples are summarized in Figures S6−S8. The electrical conductivity decreases with increasing temperature for most of the compositions, indicating that these alloys are heavily doped, in fact, degenerately doped semiconductors. These compositions hence exhibit metallic electrical conductivity behavior, with the Fermi level situated among allowed states and in a region with finite density of states. Because Fe^{2+} substitution on the Co site and the Yb^{2+} filler function as an electron acceptor and donor, respectively, the electrical conductivity decreases with increasing Fe content but increases with increasing Yb content. The FFL of Yb increased because of the charge compensation balance mechanism. For instance, $Yb_{0.25}Co_{3.9}Fe_{0.1}Sb_{12}$ and $Yb_{0.5}Co_{3.75}Fe_{0.25}Sb_{12}$ yield similar σ yet twice the increment of Yb-filling fraction, from 0.25 to 0.5. The observed increase in electrical conductivity is also consistent with the Hall effect and magnetotransport measurements. When Yb/Fe < 1:1, for example, samples #6 (Yb/Fe = 1:2), #12 (Yb/Fe = 3:5), and #18 (Yb/Fe = 4:5), σ increases with increasing temperature, indicating an occurrence of a transition to semiconducting behavior, characterized by nondegenerate doping, with the Fermi level now situated in an energy gap. Thus, a stronger bipolar effect was observed for these samples because both electrons and holes were present at elevated temperature. The Seebeck coefficient was negative for most samples, and the absolute values of S ($|S|$) increase almost linearly with a temperature up to 850 K. One exception was sample #6 because it converted to a p-type semiconductor due to a very low Yb/Fe ratio, as shown in Figure 2b. On the other hand, the bipolar effect leads to the reduction of $|S|$ with increasing temperatures above 600 K for those samples that show gapped nondegenerate semiconducting behavior, which further results in the relatively poor TE performance at high temperatures because of the mixed-electron and hole carrier transport in the conduction band, as shown in Figure S5. Overall, our Fe-substitution samples show the advantages of maximum $|S|$ shifting to a lower temperature range of 740−780 K.

Figure 3 shows the total thermal conductivity as a function of Fe content for selected $Yb_xCo_{4-y}Fe_ySb_{12}$ samples. Combined with Figure S9, the lattice thermal conductivity generally decreases with either increasing Fe content or increasing Yb content, which is consistent with previous results.[40,80,81] The increase of $\kappa_{lattice}$ for high Fe-content compositions possibly originates from the extremely high lattice thermal conductivity of $FeSb_2$ as a secondary phase.[82,83] Meanwhile, κ_e is only dependent on the carrier concentration because it decreases with increasing Fe content and increases with increasing Yb content. The ratio of κ_e/κ_{total} varies from a minimum of ∼10% (sample #18) to ∼50% (sample #19) according to different carrier concentrations. The lattice thermal conductivity basically obeys a T^{-1} relation until the involvement of bipolar thermal transport above ∼600 K, indicating the predominance of Umklapp scattering processes. The bipolar effects are

DOI: 10.1021/acs.chemmater.8b03994
Chem. Mater. 2019, 31, 862−872

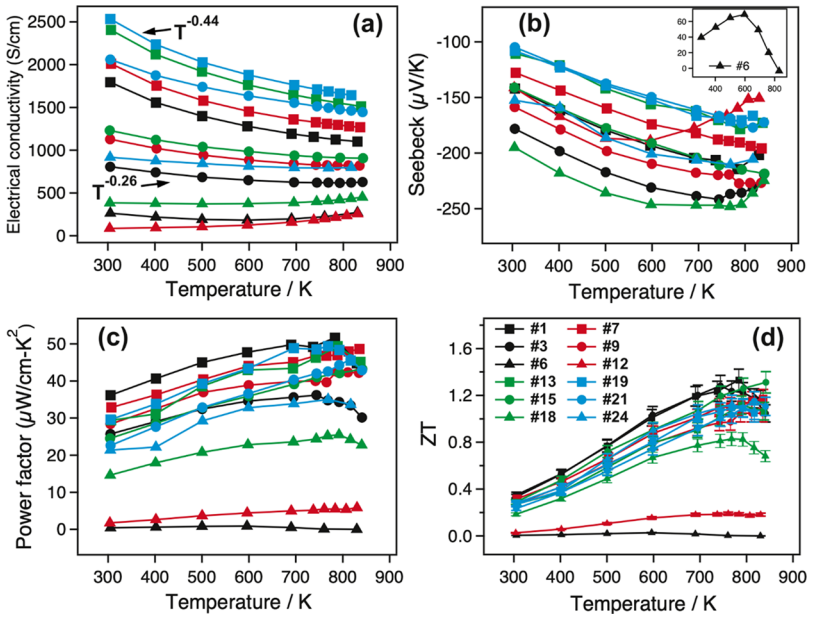

Figure 2. (a–d) Temperature dependence of (a) electrical conductivity of selected $Yb_xCo_{4-y}Fe_ySb_{12}$, (b) Seebeck coefficient of selected $Yb_xCo_{4-y}Fe_ySb_{12}$, (c) power factor of selected $Yb_xCo_{4-y}Fe_ySb_{12}$, and (d) figures of merit of selected $Yb_xCo_{4-y}Fe_ySb_{12}$ samples with ±7% error bars. The inset in (b) is the Seebeck coefficient of sample #6, which shows a positive value leading to p-type behavior. The detailed compositions can be found in Table S1.

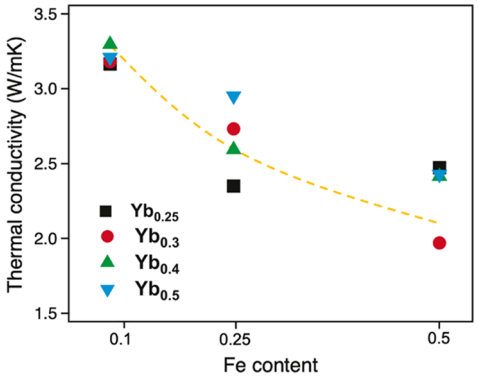

Figure 3. Total thermal conductivity as a function of Fe content for selected $Yb_xCo_{4-y}Fe_ySb_{12}$ samples.

significant for low Yb-content and high Fe-content compositions because of the increased hole concentrations resulting from Fe substitution, for example, samples #6, #12, #18, and #24. The lowest lattice thermal conductivity at room temperature was found to be ~1.4 W/m·K, which is one of the lowest values reported in the literature.[27,34,73,84]

As shown in Figure 2d and Figure S10, most of the compositions exhibit a temperature-dependent ZT between 0.3 at 300 K and 1.35 at 700–800 K. Maximum ZT values reach 1.33 for $Yb_{0.25}Co_{3.9}Fe_{0.1}Sb_{12}$ (sample #1) at 780 K, 1.28 for $Yb_{0.25}Co_{3.75}Fe_{0.25}Sb_{12}$ (sample #3) at 740 K, and 1.34 for $Yb_{0.4}Co_{3.8}Fe_{0.2}Sb_{12}$ (sample #14) at 780 K. We noticed a significant shift of ZT_{max} from ~850 K[17,19,34,71] to the range between 750 and 800 K, which will enhance ZT_{avg}, leading to the potential improvement of efficiencies of segmented and cascaded thermoelectric devices.

3. DISCUSSION

3.1. Electronic Transport Characterization upon Fe Substitution. Among all the $Yb_xCo_{4-y}Fe_ySb_{12}$ samples, the |S| of sample #5 ($Yb_{0.25}Co_{3.6}Fe_{0.4}Sb_{12}$) is the lowest (Figure S7), and only sample #6 ($Yb_{0.25}Co_{3.5}Fe_{0.5}Sb_{12}$) exhibits a positive S, as plotted in the inset of Figure 2b. This behavior marks the transition from n-type to p-type doping. The electron transport shows a complex dependence on the Co/Fe ratio due to a subtle interplay between the hole doping by Fe and the influence of the filler concentration. As Chen et al.[42] and Morelli et al.[40] proposed, the carrier concentration per formula unit of our $Yb_xCo_{4-y}Fe_ySb_{12}$ can be modified and given by $(p,n) = 4 - (4 - y) - 2x = y - 2x$. When this quantity is negative, the sample will be n-type, whereas the sample will be p-type when the equation results in a positive value. In our studies, $(p,n)_{\#5}$ equals −0.1 to −0.15, as calculated by nominal and actual compositions, whereas $(p.n)_{\#6}$ gives slightly positive values of 0 to 0.05, as shown in Figure 4. Thus, our samples are generally consistent with the above calculations. Sample #12 indicates that a small offset might occur for the (p,n) values very close to 0.

The electrical conductivities of all degenerately doped samples closely follow a power law relation with temperature ($\sigma \approx T^s$), where the temperature exponent s evolves gradually from −0.44 to −0.26, as shown in Figure 2a. Such values for the exponent s are atypical for degenerately doped semiconductors at higher temperatures above their Debye temperature. A comparison shows that, in Bi_2Te_3[85] and PbTe,[86] $-1.5 < s < -2$ (typical for lattice scattering), denoting that, in Bi_2Te_3 and PbTe, σ decreases faster with increasing temperature. The low values for the exponent s in our degenerately doped samples can be ascribed to dominance of, for example, impurity or point-defect scattering, particularly from the chemical substitution of Fe on the Co site. On the other hand, the behavior can be attributed to rapid carrier concentration changes with temperature.[87] Unlike those typical extrinsic semiconductors showing weak temperature-dependent carrier concentration, such as Bi_2Te_3[85] and PbTe,[86] the n_H of filled skutterudites strongly correlates to rising temperature

DOI: 10.1021/acs.chemmater.8b03994
Chem. Mater. 2019, 31, 862–872

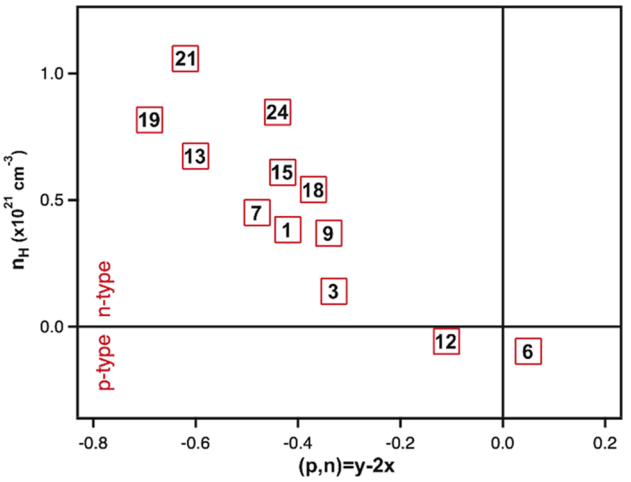

Figure 4. Carrier concentration as a function of (p,n) = $y - 2x$ for $Yb_xCo_{4-y}Fe_ySb_{12}$. The x and y values used for calculation are actual compositions from Table S2.

from ~10^{19} cm^{-3} at 300 K to ~10^{21} cm^{-3} at 850 K.[34,47,87] Fillers contribute their valence electrons as electron donors after being inserted into the nanocages of the $CoSb_3$ lattice. However, as reported by Shi et al.,[88] these fillers tend not to transfer all valence electrons to the neighboring Sb atoms at room temperature because of the nonpure-ionic bonding between fillers and Sb atoms, where Yb shows effective charge states of +1.73 to 1.76. Then, the increase of n_H with increasing temperature could correlate with the gradual ionization of Yb with increasing temperature, leading to an increased effective charge state much closer to +2. The decreasing rate of change of electrical conductivity for our compositions is also smaller than that of reported $CoSb_3$, for example, $Yb_xCo_4Sb_{12}$ ($T^{-0.66}$ to $T^{-0.51}$).[34] Figure 5a shows the room-temperature mobility as a function of carrier concentration. Single-, double-, and multi-filled $CoSb_3$ skutterudites present similar mobility values at a fixed carrier concentration, whereas Te- and Pd-doped $CoSb_3$ on the Sb site and Fe-substituted skutterudites possess smaller μ_H values at a given n_H. Because fillers hardly weaken the electron transport in skutterudites, Fe substitution must be considered to affect transport in other ways, for example, by changing the effective mass. On the basis of a simple parabolic band model and an energy-independent scattering approximation, the Seebeck coefficient for degenerate semiconductors is given by eq 1[89]

$$S = \frac{8\pi^2 k_B^2}{3eh^2} m^* T \left(\frac{\pi}{3n_H}\right)^{2/3} \quad (1)$$

where n_H is the carrier concentration, m^* is the effective mass of the carrier, and k_B, e, h, and T are the Boltzmann constant, unit charge, Planck constant, and absolute temperature, respectively. To compare the relative change of m^* with the increase of Yb and Fe content at room temperature, we use the ratio of Seebeck coefficients of two different samples

$$\frac{m_i^*}{m_j^*} = \frac{s_i}{s_j}\left(\frac{n_{Hi}}{n_{Hj}}\right)^{2/3} \quad (2)$$

where i and j represent the sample number. We found that the ratio of m_i^*/m_j^* is close to 1 at a given Fe content, indicating that m^* stays essentially constant with increasing Yb content. Figure 5b shows the effective mass ratio between selected samples at a fixed Yb content, where m_{13}^* is set as the fundamental mass and equals unity. The ratio m^*/m_{13}^*

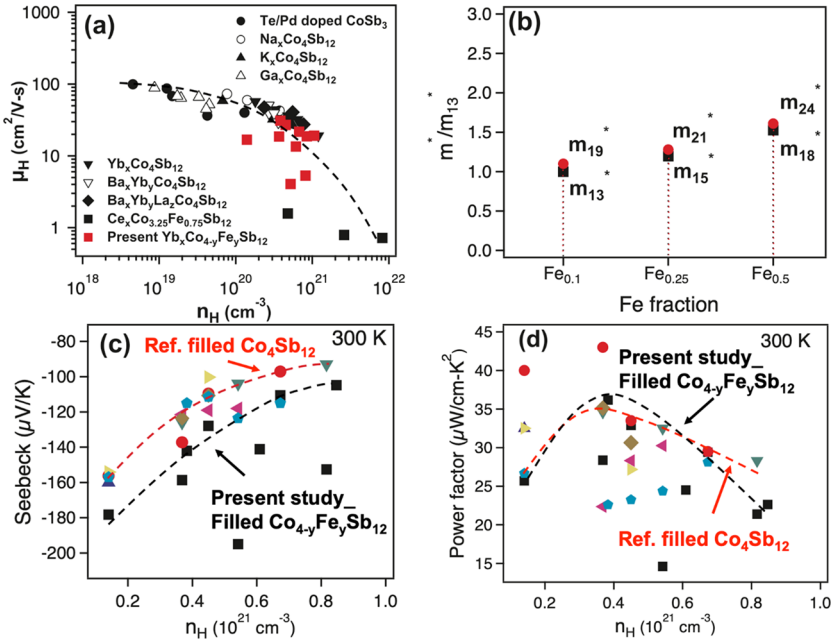

Figure 5. (a) Carrier concentration dependence of electron mobility in a filled skutterudite. The reference data are from refs 15, 27, 33, 34, 73, 87, and 90. (b) Effective mass ratio between selected samples and sample #13, where the effective mass of sample #13 is set as fundamental mass and equals to 1. The applied calculation formula can be found in eqs 1 and 2. (c, d) Carrier concentration dependence of (c) Seebeck coefficient and (d) power factor at 300 K. Black spots are from the present study with filled $Co_{4-y}Fe_ySb_{12}$ compositions. Colorful spots are from reference filled Co_4Sb_{12} compositions. Data for colorful spots are taken from refs 15, 27, 33, 34, 73, 87, and 90. The dash line is a guide to the eye. The detailed compositions can be found in Table S1.

DOI: 10.1021/acs.chemmater.8b03994
Chem. Mater. 2019, 31, 862−872

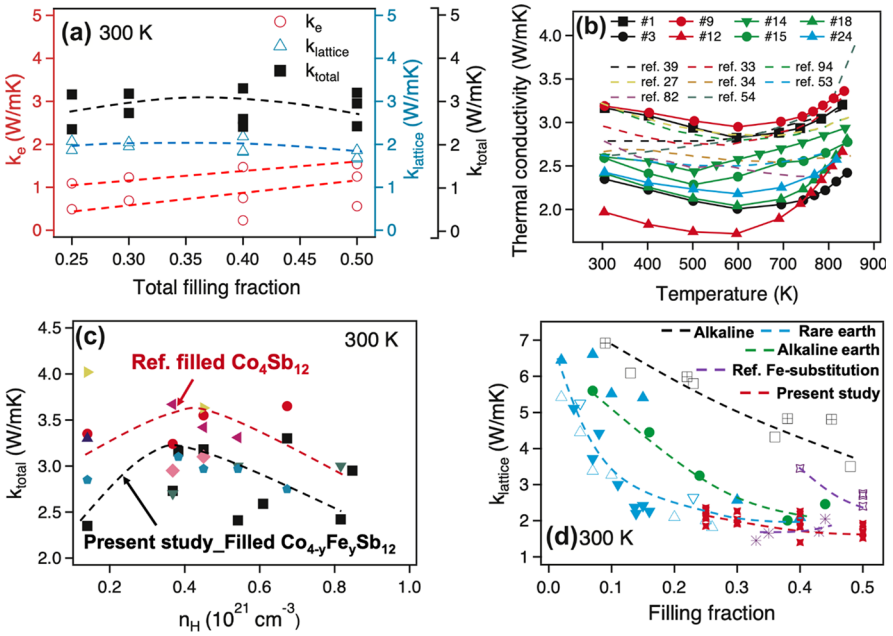

Figure 6. (a) Yb total filling fraction dependence of electron, lattice, and total thermal conductivities of selected $Yb_xCo_{4-y}Fe_ySb_{12}$ samples at 300 K. (b) Temperature dependence of total thermal conductivities of selected $Yb_xCo_{4-y}Fe_ySb_{12}$ samples and single- and multi-filled $CoSb_3$. Data for dash lines are taken from refs 27, 33, 34, 39, 53, 54, 82, and 94. (c) Carrier concentration dependence of total thermal conductivities at 300 K. Black spots are from the present study with filled $Co_{4-y}Fe_ySb_{12}$ compositions. Colorful spots are from reference filled Co_4Sb_{12} compositions. The dash line is a guide to the eye. (d) Filling fraction dependence of lattice thermal conductivities at 300 K. Filled red stars are from the present study with filled $Co_{4-y}Fe_ySb_{12}$ compositions. Colorful spots are from reference filled Co_4Sb_{12} compositions. The dash line is a guide to the eye. All the data for colorful spots are taken from refs 15, 27, 33, 34, 73, 87, and 90. The detailed compositions can be found in Table S1.

increases up to ~1.6 when the Fe content is increased from 0.1 to 0.5, indicating that the change of m^* is positively correlated with the Fe content. The trade-off trends between σ and S are always a barrier to the enhancement of TE properties. As reported by Ballikaya et al.,[53] the decrease of carrier mobility with the increase of Fe content is very limited above 300 K. Although Fe substitution cannot alter this inverse trend completely, the heavily doped $Co_{4-y}Fe_ySb_{12}$ matrix is still able to provide greater S value by offering larger m^*, leading to a decent power factor compared to the $CoSb_3$ matrix,[15,27,33,34,73,87,90] as shown in Figure 5c. Figure 5d also exhibits a competitive power factor for carrier concentrations in the range of 3.5×10^{20} to 5×10^{20} cm^{-3} for our filled $Co_{4-y}Fe_ySb_{12}$ samples. Those relative low PF values originate from the decrease of σ due to Fe substitution. According to the effective charge states of filler calculation from previous works,[27,31,88,91] if the effective charge state (q_v) of the fillers is +1, then the optimum total filling fraction (x_{total}) should be ~0.33−0.7. In our filled $Co_{4-y}Fe_ySb_{12}$ matrix, q_v is Fe-dependent, which equals to $2 - y$, where y = 0.1−0.5. Thus, the optimum x_{total} in our system lies between 0.17 and 0.47. This encapsulates why we select x between 0.25 and 0.5.

3.2. Ultralow Thermal Conductivity. The thermoelectric properties are dependent on variable processing parameters,[92] as discussed in Supporting Information. The ultralow thermal conductivities are determined by both compositional design and synthesis process. Figure 6a shows that the electronic thermal conductivity increases with an increasing Yb-filling fraction at room temperature, for example, from ~0.5 W/m·K at x = 0.25 to ~1.3 W/m·K at x = 0.5. Nevertheless, our $Yb_xCo_{4-y}Fe_ySb_{12}$ samples still show the lowest κ_{total} over the entire temperature range (almost ~10% lower) at given carrier concentrations compared to previous Yb-filled $CoSb_3$,[27,33,34,39,93] as shown in Figure 6b,c. The specific heat (C_p) used for κ_{total} calculations in our study is temperature-dependent from 0.22 to 0.25 $J \cdot g^{-1} \cdot K^{-1}$, higher than that used for triple-filled skutterudite (~0.22 $J \cdot g^{-1} \cdot K^{-1}$).[27] Another factor that could account for the lower κ_{total} is the microstructure where the filled $CoSb_3$ sample exhibits nanosized grains.[33,39,93] Our samples, as discussed above, consist of grains with an average size of ~2 μm. The lowest κ_{total} reported in the literature from triple-filling samples can be attributed primarily to the broad-frequency phonon scattering by different fillers.[27] The low κ_{total} in our work is ascribed to two effects: (1) Yb-filler rattling scattering and (2) Fe substitution on the Co site. Yb-related rattling patterns (low-lying optical phonon branches) occurring at low frequencies in the range of ~40−45 cm^{-1} due to its small radius and heavy mass lead to the specific features of its phonon dispersion.[34] Both the enhanced optical and acoustic phonon interactions and strong anharmonic lattice dynamics can contribute to reduced lattice thermal conductivity.[27,34,94] As apparent from Figure 6d, our high Yb-filling fraction is quite effective in reducing $\kappa_{lattice}$ compared to the literature results,[15,27,33,34,73,87,90] having substantially more effect than alkali and alkaline earth fillers. On the other hand, according to ab initio calculations based on molecular dynamics simulations reported by Kim et al.,[95] filling into nanocages can increase the short Sb−Sb bond on the Sb_4 ring. Such bond softening can strongly influence the phonon density of states and overall vibration spectrum, leading to flattening of the acoustic branches and a reduction in the cut-off frequency, which further results in a significant drop of the group velocity of acoustic and optical branches. Thus, as shown in Figure 3, $\kappa_{lattice}$ decreases with increasing Yb content at a given Fe content. Figure 3c shows that total thermal conductivity

DOI: 10.1021/acs.chemmater.8b03994
Chem. Mater. 2019, 31, 862−872

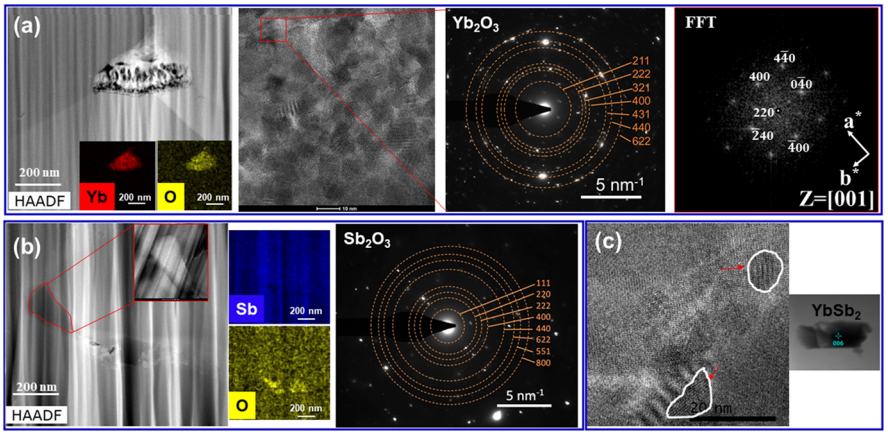

Figure 7. (a) High-angle annular dark field (HAADF) STEM image of Yb_2O_3 secondary phase, high-resolution TEM (HRTEM) image of Yb_2O_3 grains within particle, corresponding selected-area electron diffraction pattern (SAED) with overlaid rings corresponding to d-spacings for cubic Yb_2O_3 crystal structure, and fast Fourier transform analysis (FFT) from a single grain indexed for cubic structure. (b) HAADF STEM image of Sb_2O_3 secondary phase particle, EDS mapping and spectrum, and SAED pattern with overlaid rings corresponding to d-spacings for Sb_2O_3 cubic structure. (c) TEM image of $YbSb_2$ secondary phase particle. The diffraction spots not on the rings come from the $CoSb_3$ matrix.

decreases with the increase of Fe content at constant Yb concentration, which could result from the change of vibrational spectrum of Sb_4 ring due to Fe substitution on the Co site and the interaction between Fe substitution and fillers.

The phonon scattering mechanisms include Umklapp phonon−phonon processes, phonon−boundary scattering, phonon−impurity scattering, phonon−secondary phase scattering, and phonon−electron scattering. Each scattering mechanism can be described by the relaxation rate $1/\tau$, which is the inverse of the corresponding relaxation time. The total phonon scattering process can be characterized as

$$\frac{1}{\tau_t} = \frac{1}{\tau_U} + \frac{1}{\tau_B} + \frac{1}{\tau_M} + \frac{1}{\tau_{sec}} + \frac{1}{\tau_{ph\text{-}e}} \tag{3}$$

where τ_U, τ_B, τ_M, τ_{sec}, and $\tau_{ph\text{-}e}$ are due to Umklapp scattering, boundary scattering, mass fluctuation impurity scattering, secondary phase impurity scattering, and phonon−electron scattering, respectively. As shown in Figure 3, $\kappa_{lattice}$ basically follows a T^{-1} relation up to the temperature where bipolar thermal transport occurs, indicating the predominant Umklapp process, which is also the dominant scattering mechanism for degenerately doped semiconductors. According to Stokes et al.,[81] the estimated effective intrinsic relaxation rate of $1/\tau_U$ is $\sim 3 \times 10^{12}$ s^{-1} in $Co_{1-x}Fe_xSb_3$ near the Debye temperature (θ). When the extrinsic relaxation rates ($1/\tau_B$, $1/\tau_M$, $1/\tau_{sec}$, and $1/\tau_{ph\text{-}e}$) are comparable to the intrinsic U process, they act as major contributors for the reduction of thermal conductivity. Grain boundary scattering and mass fluctuation impurity scattering, with the relaxation rate of $\sim 10^9$ s^{-1} range, show negligible influence on the reduction of total thermal conductivity (as discussed in Supporting Information). The in situ-formed nanoinclusions, for example, Yb_2O_3, Sb_2O_3, $YbSb_2$, and $FeSb_2$, with a size distribution between a few nanometers and 100 nm, as shown in Figure 7 (EDS spectra can be found in Figure S11), effectively scatter both short-range and long-range acoustic phonons and reduced thermal conductivity. Meanwhile, phonon−electron scattering turns out to be the major source in our study, leading to the ultralow thermal conductivity, which was not found to be significant in other studies on related compositions. The phonon−electron scattering term, of which the relaxation rate is given by eq 4[96] (for $T = \theta$), is as follows

$$\frac{1}{\tau_{ph\text{-}e}} = \frac{n_H{}^2 e^2 \upsilon^2}{N k_B T \sigma \varphi} \tag{4}$$

$$\varphi = 4^3 (6\pi)^{1/2} (\upsilon m^* \delta / h)^{3/2} \tag{5}$$

where N is the Avogadro's number and φ is described in eq 5. By using our experimental data, a phonon−electron relaxation rate of $\sim 10^{12}$−10^{13} s^{-1} is obtained, which is comparable to the intrinsic U process relaxation rate estimated above and could be the major source of the decrease of thermal conductivity. The phonon−electron scattering, which is also called phonon drag, is mostly predominant at low temperature ($\sim {}^1/_5\theta$),[97,98] but is limited at room temperature and above. A possible speculation is the mixed valence state effect from phonon−electron interactions.[40] The zero-spin Fe^{2+} d^6 configuration is well known to be a somehow energetically unstable state in similar materials such as FeS_2. Thus, a scenario is that a traveling phonon can be scattered or absorbed by a dynamic exchange of electrons transferred from one Fe^{2+} to a neighboring Co^{3+}. A similar phenomenon was observed in Fe_3O_4 above 119 K where a rapid phonon-assisted exchange of electrons between Fe^{2+} and Fe^{3+} leads to the drop of thermal conductivity.[99] In $Yb_xCo_{4-y}Fe_ySb_{12}$ samples, because each unit cell of volume $a_0{}^3$ contains eight possible metal atom sites in a skutterudite structure, $c(Co^{3+}) = 8(4 - y)/a_0{}^3$ and $c(Fe^{2+}) = 8y/a_0{}^3$, so the trend of phonon scattering by dynamic exchange of electrons could be estimated[100] as in eq 6

$$\kappa_{total} \propto 1/D = \frac{1}{[c(Co^{3+})] \times [c(Fe^{2+})]} = \frac{a_0{}^6}{64(4 - y)y} \tag{6}$$

where D is defined as the concentration parameter, which reaches a maximum value when $y = 2$. Therefore, this dynamic exchange of electron scattering on phonons becomes stronger and stronger, leading to a lower thermal conductivity with increasing Fe content up to $y = 2$.

3.3. Shift of ZT_{max} to Lower Temperature. Figure 2d shows a distinct shift in ZT_{max} from 850 K to the range of 740−780 K. As mentioned previously, lower temperatures for

DOI: 10.1021/acs.chemmater.8b03994
Chem. Mater. 2019, 31, 862−872

ZT_{max} are required for skutterudites to fully utilize their performance in multistage devices. In our study, ZT_{max} values of 1.33, 1.28, and 1.34 for samples #1, #3, and #14 were achieved in the temperature range of 740−780 K, as shown in Figure 2d and Figure S10. These results are comparable to the highest recorded values[27,34,101] so far and more than 10% higher than most ZT values[33,73,84,87,90,102,103] at similar temperatures. The shift of ZT_{max} can be ascribed to the proper holes introduced into the $CoSb_3$ matrix by Fe substitution on the Co site that shifts the temperature at which the peak Seebeck coefficient and power factor appear between 740 and 780 K as a result of the nonharmful bipolar effect. Moreover, the lowest thermal conductivities mostly appear at around 600 K, as shown in Figure S9. The further shift of the maximum Seebeck coefficient and power factor into this temperature range without deterioration of electron transport is promising and will be the subject of future research.

4. CONCLUSIONS

In this study, we demonstrate (1) an enhanced filling fraction limitation of Yb-single filler from low values of 0.2−0.3 to a high value of 0.5 due to the charge balance compensation mechanism, (2) increased effective mass leading to the increase of the absolute value of the Seebeck coefficient by ∼10−12.5%, and (3) ultralow thermal conductivities resulting from secondary phases and phonon−electron scattering, as low as ∼1.75 W/m·K. These are the lowest values reported so far from not only single filling but also double and multi-filling. Another important result is that the temperature at which the maximum ZT value appears shifts from 850 K down to 740−780 K. Finally, we measured a high ZT value of 1.34 around 750 K, one of the highest values reported at this temperature and comparable to the best results for skutterudites. This combination of a large ZT value at a lower temperature is an important step toward wider use of skutterudites in practical multistage thermoelectric devices.

5. EXPERIMENTAL PROCEDURES

5.1. Sample Preparation. The Yb-single-filling skutterudite with Fe substitution on Co-site sample $Yb_xCo_{4-y}Fe_ySb_{12}$ (x = 0.25, 0.3, 0.4, 0.5; y = 0.1, 0.2, 0.25, 0.3, 0.4, 0.5) was synthesized by traditional melting, followed by quenching and long-term high-temperature annealing. From this point onward, the compositions are termed as Yb series and Fe series, as shown in Table S1 (Supporting Information). The high-purity nonpowder elements Yb (99.9%, chips), Co (99.9%, pieces), Fe (99.99%, pieces), and Sb (99.9999%, shot) were weighed inside a glove box in their corresponding stoichiometric ratios and filled into quartz tubes with graphite coatings inside. The tubes were then sealed under high vacuum, and the materials were melted at 1060 °C for 20 h. The resulting melts were quenched by NaCl-saturated ice water at room temperature, annealed at 700 °C for 1 week, and then hand-ground into fine powder below 75 μm. The resulting powders were consolidated by spark plasma sintering (SPS, Fuji SPS-615) at 650 °C under a pressure of 40 MPa for 5 min, yielding fully densified bulk pellets.

5.2. Structural Characterization. Room-temperature powder X-ray diffraction (XRD) data were collected on a Bruker D8 diffractometer with Cu Kα radiation (λ = 1.5418 Å) to check the phase purity. The refinement by Rietveld analysis was applied for all of the compositions using the FullProf program. The actual compositions were determined by scanning electron microscopy (FEI Quanta 600 FEG) averaged over 18 randomly selected points via energy-dispersive X-ray spectroscopy (EDS). A transmission electron microscope (TEM; FEI Titan 300 and Talos F200X with Super-X detector) was employed to examine the microstructure of the sample. The diffraction pattern analysis was done using the JEMS software.

5.3. Thermoelectric Transport Properties. The transverse resistance (R_{XY}, Hall resistance) and longitudinal resistance (sheet resistance) were measured in a dedicated magnetotransport setup at room temperature (297 K) using four-contact van der Pauw sample configurations. Magnetotransport results were obtained over magnetic fields (B) up to ±1.4 T using a lock-in amplifier to measure the voltage signals under 10 mA rms current excitation. Linearity of the current−voltage characteristics of the ohmic contacts was ascertained up to 20 mA excitation current. The electrical conductivity and Seebeck coefficient were measured simultaneously from room temperature to 850 K using an ULVAC-RIKO ZEM-3 system. High-temperature thermal properties were determined by measuring thermal diffusivity with a laser flash system (ULVAC-RIKO TC-1200RH). Specific heat was measured with a differential scanning calorimeter (Netzsch DSC 404C). Finally, thermal conductivity, κ, was calculated from $\kappa = \alpha\rho C_p$, where α is the thermal diffusivity, ρ is the density, and C_p is the specific heat. The uncertainties in electrical conductivity, thermal conductivity, Seebeck coefficient, and ZT are ±5, ±2, ±5, and ±7%, respectively.

■ ASSOCIATED CONTENT

Supporting Information

The Supporting Information is available free of charge on the ACS Publications website at DOI: 10.1021/acs.chemmater.8b03994.

Schematic demonstration of multistage TE device, compositions and density/Seebeck coefficient/electrical conductivity/total thermal conductivity/carrier concentration/carrier mobility at room temperature, X-ray diffraction pattern for all samples, elemental mapping images for selected Yb-rich samples, schematic diagram of bipolar effect, additional ultralow thermal conductivity analysis, temperature dependence of electrical conductivity/Seebeck coefficient/power factor/thermal conductivity/ZT for all the samples, and EDS spectra of secondary phases (PDF)

■ AUTHOR INFORMATION

Corresponding Authors

*E-mail: wzl175@psu.edu (W.L.).
*E-mail: sup103@psu.edu (S.P.).

ORCID

Wenjie Li: 0000-0003-4509-3303
Jean J. Heremans: 0000-0002-6346-8597

Notes

The authors declare no competing financial interest.

■ ACKNOWLEDGMENTS

The authors thank Christopher Winkler for the experimental data of HRTEM. This work was supported by the office of Defense Advanced Research Projects Agency (DARPA) under the project of Nano Engineered Thermoelectric Systems (NETS).

■ REFERENCES

(1) Muto, A.; Yang, J.; Poudel, B.; Ren, Z.; Chen, G. Skutterudite Unicouple Characterization for Energy Harvesting Applications. *Adv. Energy Mater.* **2013**, *3*, 245−251.

(2) Chu, S.; Majumdar, A. Opportunities and challenges for a sustainable energy future. *Nature* **2012**, *488*, 294−303.

(3) Yang, J.; Caillat, T. Thermoelectric materials for space and automotive power generation. *MRS Bull.* **2006**, *31*, 224−229.

DOI: 10.1021/acs.chemmater.8b03994
Chem. Mater. 2019, 31, 862−872

(4) Champier, D. Thermoelectric generators: A review of applications. *Energy Convers. Manage.* **2017**, *140*, 167−181.
(5) Uher, C. Skutterudites: Promising power conversion thermoelectrics. In *Proceedings of the 22nd International Conference on Thermoelectrics*; IEEE, 2003; pp 42−47.
(6) Tritt, T. M. Thermoelectric Phenomena, Materials, and Applications. *Annu. Rev. Mater. Res.* **2011**, *41*, 433−448.
(7) Shields, V.; Caillat, T.; Fleurial, J. P.; Zoltan, A.; Zoltan, L.; Tuchscherer, M. Synthesis and thermoelectric properties of $Co_{1-x}Ni_xP_3$ and $CoAs_{3-x}P_x$. In *Proceedings of the 21st International Conference on Thermoelectrics*; IEEE, 2002; pp 64−67.
(8) Peranio, N.; Eibl, O.; Bäßler, S.; Nielsch, K.; Klobes, B.; Hermann, R. P.; Daniel, M.; Albrecht, M.; Görlitz, H.; Pacheco, V.; Bedoya-Martínez, N.; Hashibon, A.; Elsässer, C. From thermoelectric bulk to nanomaterials: Current progress for Bi_2Te_3 and $CoSb_3$. *Phys. Status Solidi A* **2016**, *213*, 739−749.
(9) Wu, H. J.; Zhao, L.-D.; Zheng, F. S.; Wu, D.; Pei, Y. L.; Tong, X.; Kanatzidis, M. G.; He, J. Q. Broad temperature plateau for thermoelectric figure of merit ZT>2 in phase-separated $PbTe_{0.7}S_{0.3}$. *Nat. Commun.* **2014**, *5*, 4515.
(10) Nolas, G. S.; Morelli, D. T.; Tritt, T. M. Skutterudites: A phonon-glass-electron crystal approach to advanced thermoelectric energy conversion applications. *Annu. Rev. Mater. Sci.* **1999**, *29*, 89−116.
(11) Snyder, G. J.; Toberer, E. S. Complex thermoelectric materials. *Nat. Mater.* **2008**, *7*, 105−114.
(12) Sales, B. C.; Mandrus, D.; Williams, R. K. Filled skutterudite antimonides: A new class of thermoelectric materials. *Science* **1996**, *272*, 1325−1328.
(13) Rotter, M.; Rogl, P.; Grytsiv, A.; Wolf, W.; Krisch, M.; Mirone, A. Lattice dynamics of skutterudites: Inelastic x-ray scattering on $CoSb_3$. *Phys. Rev. B* **2008**, *77*, 144301.
(14) Luo, H.; Krizan, J. W.; Muechler, L.; Haldolaarachchige, N.; Klimczuk, T.; Xie, W.; Fuccillo, M. K.; Felser, C.; Cava, R. J. A large family of filled skutterudites stabilized by electron count. *Nat. Commun.* **2015**, *6*, 6489.
(15) Tang, Y.; Gibbs, Z. M.; Agapito, L. A.; Li, G.; Kim, H.-S.; Nardelli, M. B.; Curtarolo, S.; Snyder, G. J. Convergence of multi-valley bands as the electronic origin of high thermoelectric performance in $CoSb_3$ skutterudites. *Nat. Mater.* **2015**, *14*, 1223−1228.
(16) Ballikaya, S.; Uzar, N.; Yildirim, S.; Chi, H.; Su, X.; Tan, G.; Tang, X.; Uher, C. Lower Thermal Conductivity and Higher Thermoelectric Performance of Fe-Substituted and Ce, Yb Double-Filled p-Type Skutterudites. *J. Electron. Mater.* **2012**, *42*, 1622−1627.
(17) Duan, B.; Yang, J.; Salvador, J. R.; He, Y.; Zhao, B.; Wang, S.; Wei, P.; Ohuchi, F. S.; Zhang, W. Q.; Hermann, R. P.; Gourdon, O.; Mao, S. X.; Cheng, Y.; Wang, C.; Liu, J.; Zhai, P.; Tang, X.; Zhang, Q.; Yang, J. Electronegative guests in $CoSb_3$. *Energy Environ. Sci.* **2016**, *9*, 2090−2098.
(18) Meisner, G. P.; Morelli, D. T.; Hu, S.; Yang, J.; Uher, C. Structure and lattice thermal conductivity of fractionally filled skutterudites: Solid solutions of fully filled and unfilled end members. *Phys. Rev. Lett.* **1998**, *80*, 3551−3554.
(19) Tang, Y.; Qiu, Y.; Xi, L.; Shi, X.; Zhang, W.; Chen, L.; Tseng, S.-M.; Chen, S.-w.; Snyder, G. J. Phase diagram of In−Co−Sb system and thermoelectric properties of In-containing skutterudites. *Energy Environ. Sci.* **2014**, *7*, 812−819.
(20) Xi, L.; Qiu, Y.; Zheng, S.; Shi, X.; Yang, J.; Chen, L.; Singh, D. J.; Yang, J.; Zhang, W. Complex doping of group 13 elements In and Ga in caged skutterudite $CoSb_3$. *Acta Mater.* **2015**, *85*, 112−121.
(21) Yang, J.; Zhang, L.; Liu, Y.; Chen, C.; Li, J.; Yu, D.; He, J.; Liu, Z.; Tian, Y.; Xu, B. Investigation of skutterudite $Mg_yCo_4Sb_{12}$: High pressure synthesis and thermoelectric properties. *J. Appl. Phys.* **2013**, *113*, 113703.
(22) Yan, Y. G.; Wong-Ng, W.; Li, L.; Levin, I.; Kaduk, J. A.; Suchomel, M. R.; Sun, X.; Tan, G. J.; Tang, X. F. Structures and thermoelectric properties of double-filled $(Ca_xCe_{1-x})Fe_4Sb_{12}$ skutterudites. *J. Solid State Chem.* **2014**, *218*, 221−229.
(23) Mei, Z. G.; Yang, J.; Pei, Y. Z.; Zhang, W.; Chen, L. D.; Yang, J. Alkali-metal-filled $CoSb_3$ skutterudites as thermoelectric materials: Theoretical study. *Phys. Rev. B* **2008**, *77*, 045202.
(24) Slack, G. A. *CRC Handbook of Thermoelectrics*; CRC Press, 1995.
(25) Keppens, V.; Mandrus, D.; Sales, B. C.; Chakoumakos, B. C.; Dai, P.; Coldea, R.; Maple, M. B.; Gajewski, D. A.; Freeman, E. J.; Bennington, S. Localized vibrational modes in metallic solids. *Nature* **1998**, *395*, 876−878.
(26) Hermann, R. P.; Jin, R.; Schweika, W.; Grandjean, F.; Mandrus, D.; Sales, B. C.; Long, G. J. Einstein oscillators in thallium filled antimony skutterudites. *Phys. Rev. Lett.* **2003**, *90*, 135505.
(27) Shi, X.; Yang, J.; Salvador, J. R.; Chi, M.; Cho, J. Y.; Wang, H.; Bai, S.; Yang, J.; Zhang, W.; Chen, L. Multiple-Filled Skutterudites: High Thermoelectric Figure of Merit through Separately Optimizing Electrical and Thermal Transports. *J. Am. Chem. Soc.* **2011**, *133*, 7837−7846.
(28) Shi, X.; Bai, S.; Xi, L.; Yang, J.; Zhang, W.; Chen, L.; Yang, J. Realization of high thermoelectric performance in n-type partially filled skutterudites. *J. Mater. Res.* **2011**, *26*, 1745−1754.
(29) Nolas, G. S.; Kaeser, M.; IV Littleton, R.; Tritt, T. M. High figure of merit in partially filled ytterbium skutterudite materials. *Appl. Phys. Lett.* **2000**, *77*, 1855−1857.
(30) Fairbanks, J. W. V. *Vehicular Thermoelectrics: A New Green Technology in Directions in Engine-Efficiency and Emission Research (DEER) Conference Presentations*, Detroit, Michigan; 2011.
(31) Shi, X.; Zhang, W.; Chen, L. D.; Yang, J. Filling fraction limit for intrinsic voids in crystals: Doping in skutterudites. *Phys. Rev. Lett.* **2005**, *95*, 185503.
(32) Mei, Z. G.; Zhang, W.; Chen, L. D.; Yang, J. Filling fraction limits for rare-earth atoms in $CoSb_3$: An ab initio approach. *Phys. Rev. B* **2006**, *74*, 153202.
(33) Yang, J.; Hao, Q.; Wang, H.; Lan, Y. C.; He, Q. Y.; Minnich, A.; Wang, D. Z.; Harriman, J. A.; Varki, V. M.; Dresselhaus, M. S.; Chen, G.; Ren, Z. F. Solubility study of Yb in n-type skutterudites $Yb_xCo_4Sb_{12}$ and their enhanced thermoelectric properties. *Phys. Rev. B* **2009**, *80*, 115329.
(34) Wang, S.; Salvador, J. R.; Yang, J.; Wei, P.; Duan, B.; Yang, J. High-performance n-type $Yb_xCo_4Sb_{12}$: From partially filled skutterudites towards composite thermoelectrics. *NPG Asia Mater.* **2016**, *8*, No. e285.
(35) Yao, Z.; Li, X. Y.; Tang, Y. S.; Chen, L. D. Genomic Effects of the Quenching Process on the Microstructure and Thermoelectric Properties of $Yb_{0.3}Co_4Sb_{12}$. *J. Electron. Mater.* **2015**, *44*, 1890−1895.
(36) Chen, Y.; Kawamura, Y.; Hayashi, J.; Sekine, C. Thermoelectric properties of $Yb_xCo_4Sb_{12}$ prepared under high pressure. *Jpn. J. Appl. Phys.* **2015**, *54*, 055501.
(37) Park, K.-H.; Seo, W.-S.; Shin, D.-K.; Kim, I.-H. Thermoelectric properties of Yb-filled $CoSb_3$ skutterudites. *J. Korean Phys. Soc.* **2014**, *65*, 491−495.
(38) Park, K.-H.; Lee, S.; Seo, W.-S.; Baek, S.; Shin, D.-K.; Kim, I.-H. Thermoelectric Properties of La-filled $CoSb_3$ Skutterudites. *J. Korean Phys. Soc.* **2014**, *64*, 1004−1008.
(39) Dahal, T.; Jie, Q.; Joshi, G.; Chen, S.; Guo, C.; Lan, Y.; Ren, Z. Thermoelectric property enhancement in Yb-doped n-type skutterudites $Yb_xCo_4Sb_{12}$. *Acta Mater.* **2014**, *75*, 316−321.
(40) Morelli, D. T.; Meisner, G. P.; Chen, B.; Hu, S.; Uher, C. Cerium filling and doping of cobalt triantimonide. *Phys. Rev. B* **1997**, *56*, 7376−7383.
(41) Uher, C. Chapter 5 Skutterudites: Prospective novel thermoelectrics. *Semicond. Semimetals* **2001**, *69*, 139−253.
(42) Chen, B.; Xu, J.-H.; Uher, C.; Morelli, D. T.; Meisner, G. P.; Fleurial, J.-P.; Caillat, T.; Borshchevsky, A. Low-temperature transport properties of the filled skutterudites $CeFe_{4-x}Co_xSb_{12}$. *Phys. Rev. B* **1997**, *55*, 1476−1480.
(43) Grytsiv, A.; Rogl, P.; Berger, S.; Paul, C.; Bauer, E.; Godart, C.; Ni, B.; Abd-Elmeguid, M. M.; Saccone, A.; Ferro, R.; Kaczorowski, D. Structure and physical properties of the thermoelectric skutterudites $Eu_yFe_{4-x}Co_xSb_{12}$. *Phys. Rev. B* **2002**, *66*, 094411.

DOI: 10.1021/acs.chemmater.8b03994
Chem. Mater. 2019, 31, 862−872

(44) Tang, X.; Zhang, Q.; Chen, L.; Goto, T.; Hirai, T. Synthesis and thermoelectric properties of p-type- and n-type-filled skutterudite $R_yM_xCo_{4-x}Sb_{12}$(R : Ce, Ba, Y; M : Fe, Ni). *J. Appl. Phys.* **2005**, *97*, 093712.
(45) Ballikaya, S.; Uher, C. Enhanced thermoelectric performance of optimized Ba, Yb filled and Fe substituted skutterudite compounds. *J. Alloys Compd.* **2014**, *585*, 168−172.
(46) Tan, G.; Zheng, Y.; Tang, X. High thermoelectric performance of nonequilibrium synthesized $CeFe_4Sb_{12}$ composite with multi-scaled nanostructures. *Appl. Phys. Lett.* **2013**, *103*, 183904.
(47) Tan, G.; Liu, W.; Wang, S.; Yan, Y.; Li, H.; Tang, X.; Uher, C. Rapid preparation of $CeFe_4Sb_{12}$ skutterudite by melt spinning: rich nanostructures and high thermoelectric performance. *J. Electron. Mater.* **2013**, *1*, 12657−12668.
(48) Geng, H.; Ochi, T.; Suzuki, S.; Kikuchi, M.; Ito, S.; Guo, J. Thermoelectric Properties of Multifilled Skutterudites with La as the Main Filler. *J. Electron. Mater.* **2013**, *42*, 1999−2005.
(49) Dong, Y.; Puneet, P.; Tritt, T. M.; Nolas, G. S. High-temperature thermoelectric properties of p-type skutterudites $Yb_xCo_3FeSb_{12}$. *Phys. Status Solidi RRL* **2013**, *7*, 418−420.
(50) Lu, P.; Lu, M.; Qu, L.; Hu, X. Effects of disordered structure on thermoelectric properties of $LaCeFe_3CoSb_{12}$ nanocomposites. *J. Mater. Res.* **2012**, *27*, 1518−1521.
(51) Choi, S.; Kurosaki, K.; Yusufu, A.; Ohishi, Y.; Muta, H.; Yamanaka, S. Thermoelectric Properties of p-Type Tl-Filled Skutterudites: $Tl_xFe_{1.5}Co_{2.5}Sb_{12}$. *J. Electron. Mater.* **2015**, *44*, 1743−1749.
(52) Chen, Y.; Kawamura, Y.; Hayashi, J.; Sekine, C. Enhanced thermoelectric performance of optimized Yb-filled and Fe-substituted skutterudite compounds $Yb_{0.6}Fe_xCo_{4-x}Sb_{12}$. *Jpn. J. Appl. Phys.* **2016**, *55*, 04EJ02.
(53) Ballikaya, S.; Uzar, N.; Yildirim, S.; Salvador, J. R. Electrical and thermal properties of Fe substituted double-filled $Ba_xYb_yFe_zCo_{4-z}Sb_{12}$ skutterudites. *J. Solid State Chem.* **2013**, *197*, 440−446.
(54) Guo, J. Q.; Geng, H. Y.; Ochi, T.; Suzuki, S.; Kikuchi, M.; Yamaguchi, Y.; Ito, S. Development of Skutterudite Thermoelectric Materials and Modules. *J. Electron. Mater.* **2012**, *41*, 1036−1042.
(55) Zhou, C.; Sakamoto, J.; Morelli, D.; Zhou, X.; Wang, G.; Uher, C. Thermoelectric properties of $Co_{0.9}Fe_{0.1}Sb_3$-based skutterudite nanocomposites with $FeSb_2$ nanoinclusions. *J. Appl. Phys.* **2011**, *109*, 063722.
(56) Tang, X.; Chen, L.; Goto, T.; Hirai, T. Effects of Ce filling fraction and Fe content on the thermoelectric properties of Co-rich $Ce_yFe_xCo_{4-x}Sb_{12}$. *J. Mater. Res.* **2001**, *16*, 837−843.
(57) Park, K.-H.; You, S.-W.; Ur, S.-C.; Kim, I.-H.; Choi, S.-M.; Seo, W.-S. High-Temperature Stability of Thermoelectric Skutterudite $In_{0.25}Co_3FeSb_{12}$. *J. Electron. Mater.* **2012**, *41*, 1051−1056.
(58) Dong, Y.; Puneet, P.; Tritt, T. M.; Martin, J.; Nolas, G. S. High temperature thermoelectric properties of p-type skutterudites $Ba_xYb_yCo_{4-z}Fe_zSb_{12}$. *J. Appl. Phys.* **2012**, *112*, 083718.
(59) Tang, X.; Li, H.; Zhang, Q.; Niino, M.; Goto, T. Synthesis and thermoelectric properties of double-atom-filled skutterudite compounds $Ca_mCe_nFe_xCo_{4-x}Sb_{12}$. *J. Appl. Phys.* **2006**, *100*, 123702.
(60) Shi, X.; Chen, L. Thermoelectric materials step up. *Nat. Mater.* **2016**, *15*, 691−692.
(61) Hu, X.; Jood, P.; Ohta, M.; Kunii, M.; Nagase, K.; Nishiate, H.; Kanatzidis, M. G.; Yamamoto, A. Power generation from nanostructured PbTe-based thermoelectrics: comprehensive development from materials to modules. *Energy Environ. Sci.* **2016**, *9*, 517−529.
(62) Zong, P.-a.; Hanus, R.; Dylla, M.; Tang, Y.; Liao, J.; Zhang, Q.; Snyder, G. J.; Chen, L. Skutterudite with graphene-modified grain-boundary complexion enhances zT enabling high-efficiency thermoelectric device. *Energy Environ. Sci.* **2017**, *10*, 183−191.
(63) Salvador, J. R.; Cho, J. Y.; Ye, Z.; Moczygemba, J. E.; Thompson, A. J.; Sharp, J. W.; Koenig, J. D.; Maloney, R.; Thompson, T.; Sakamoto, J.; Wang, H.; Wereszczak, A. A. Conversion efficiency of skutterudite-based thermoelectric modules. *Phys. Chem. Chem. Phys* **2014**, *16*, 12510−12520.
(64) Nie, G.; Suzuki, S.; Tomida, T.; Sumiyoshi, A.; Ochi, T.; Mukaiyama, K.; Kikuchi, M.; Guo, J. Q.; Yamamoto, A.; Obara, H. Performance of Skutterudite-Based Modules. *J. Electron. Mater.* **2017**, *46*, 2640−2644.
(65) Fu, C.; Bai, S.; Liu, Y.; Tang, Y.; Chen, L.; Zhao, X.; Zhu, T. Realizing high figure of merit in heavy-band p-type half-Heusler thermoelectric materials. *Nat. Commun.* **2015**, *6*, 8144.
(66) Zhang, Q. H.; Huang, X. Y.; Bai, S. Q.; Shi, X.; Uher, C.; Chen, L. D. Thermoelectric Devices for Power Generation: Recent Progress and Future Challenges. *Adv. Eng. Mater.* **2016**, *18*, 194−213.
(67) Caillat, T.; Firdosy, S.; Li, B. C.; Huang, C.-K.; Ravi, V. A.; Keyawa, N. R.; Anjunyan, H.; Paik, J.-A.; Uhl, D. M.; Chase, J.; Lara, L.; Fleurial, J.-P. Development of High Efficiency Segmented Thermoelectric Couples. In *11th International Energy Conversion Engineering Conference*, San Jose, CA; 2013.
(68) Zhang, Q.; Liao, J.; Tang, Y.; Gu, M.; Ming, C.; Qiu, P.; Bai, S.; Shi, X.; Uher, C.; Chen, L. Realizing a thermoelectric conversion efficiency of 12% in bismuth telluride/skutterudite segmented modules through full-parameter optimization and energy-loss minimized integration. *Energy Environ. Sci.* **2017**, *10*, 956−963.
(69) Sun, X.; Liang, X.; Shu, G.; Tian, H.; Wei, H.; Wang, X. Comparison of the two-stage and traditional single-stage thermoelectric generator in recovering the waste heat of the high temperature exhaust gas of internal combustion engine. *Energy* **2014**, *77*, 489−498.
(70) Lee, H.; Sharp, J.; Stokes, D.; Pearson, M.; Priya, S. Modeling and analysis of the effect of thermal losses on thermoelectric generator performance using effective properties. *Appl. Energy* **2018**, *211*, 987−996.
(71) Qiu, Y.; Xing, J.; Gao, X.; Xi, L.; Shi, X.; Gu, H.; Chen, L. Electrical properties and microcosmic study on compound defects in Ga-containing thermoelectric skutterudites. *J. Mater. Chem. A* **2014**, *2*, 10952−10959.
(72) Salvador, J. R.; Cho, J. Y.; Ye, Z.; Moczygemba, J. E.; Thompson, A. J.; Sharp, J. W.; König, J. D.; Maloney, R.; Thompson, T.; Sakamoto, J.; Wang, H.; Wereszczak, A. A.; Meisner, G. P. Thermal to Electrical Energy Conversion of Skutterudite-Based Thermoelectric Modules. *J. Electron. Mater.* **2013**, *42*, 1389−1399.
(73) Tang, Y.; Hanus, R.; Chen, S.-w.; Snyder, G. J. Solubility design leading to high figure of merit in low-cost Ce-$CoSb_3$ skutterudites. *Nat. Commun.* **2015**, *6*, 7584.
(74) Li, H.; Tang, X.; Zhang, Q.; Uher, C. Rapid preparation method of bulk nanostructured $Yb_{0.3}Co_4Sb_{12+y}$ compounds and their improved thermoelectric performance. *Appl. Phys. Lett.* **2008**, *93*, 252109.
(75) Sesselmann, A.; Klobes, B.; Dasgupta, T.; Gourdon, O.; Hermann, R.; Mueller, E. Neutron diffraction and thermoelectric properties of indium filled $In_xCo_4Sb_{12}$ (x = 0.05, 0.2) and indium cerium filled $Ce_{0.05}In_{0.1}Co_4Sb_{12}$ skutterudites. *Phys. Status Solidi A* **2016**, *213*, 766−773.
(76) Tang, Y.; Chen, S.-w.; Snyder, G. J. Temperature dependent solubility of Yb in Yb−$CoSb_3$ skutterudite and its effect on preparation, optimization and lifetime of thermoelectrics. *J. Materiomics* **2015**, *1*, 75−84.
(77) Massalsk, T. B.; Okamoto, H. Co-Yb (Cobalt-Ytterbium). In *Binary Alloy Phase Diagrams*, 2nd ed.; ASM International, 1990; Vol. 3, pp 1261−1262.
(78) Massalsk, T. B.; Okamoto, H. Sb-Yb (Antimony-Ytterbium). In *Binary Alloy Phase Diagrams*, 2nd ed.; ASM International, 1990; Vol. 3, pp 3317−3320.
(79) Okamoto, H. Co-Sb (Cobalt-Antimony). *J. Phase Equilib.* **1991**, *12*, 244−245.
(80) Katsuyama, S.; Shichijo, Y.; Ito, M.; Majima, K.; Nagai, H. Thermoelectric properties of the skutterudite $Co_{1-x}Fe_xSb_3$ system. *J. Appl. Phys.* **1998**, *84*, 6708−6712.
(81) Stokes, K. L.; Ehrlich, A. C.; Nolas, G. S. Thermal conductivity of Fe-doped $CoSb_3$ skutterudites. *MRS Online Proc. Libr.* **1998**, *545*, 339−344.

DOI: 10.1021/acs.chemmater.8b03994
Chem. Mater. 2019, 31, 862−872

(82) Sun, P.; Oeschler, N.; Johnsen, S.; Iversen, B. B.; Steglich, F. Narrow band gap and enhanced thermoelectricity in $FeSb_2$. *Dalton Trans.* **2010**, *39*, 1012−1019.
(83) Liao, B.; Lee, S.; Esfarjani, K.; Chen, G. First-principles study of thermal transport in $FeSb_2$. *J. Mater. Chem. B* **2014**, *89*, 035108.
(84) Graff, J. W.; Zeng, X.; Dehkordi, A. M.; He, J.; Tritt, T. M. Exceeding the filling fraction limit in $CoSb_3$ skutterudite: Multi-role chemistry of praseodymium leading to promising thermoelectric performance. *J. Mater. Chem. A* **2014**, *2*, 8933−8940.
(85) Wang, S.; Tan, G.; Xie, W.; Zheng, G.; Li, H.; Yang, J.; Tang, X. Enhanced thermoelectric properties of $Bi_2(Te_{1-x}Se_x)_3$-based compounds as n-type legs for low-temperature power generation. *J. Mater. Chem.* **2012**, *22*, 20943−20951.
(86) Pei, Y.; LaLonde, A. D.; Wang, H.; Snyder, G. J. Low effective mass leading to high thermoelectric performance. *Energy Environ. Sci.* **2012**, *5*, 7963−7969.
(87) Wang, S.; Yang, J.; Wu, L.; Wei, P.; Zhang, W.; Yang, J. On Intensifying Carrier Impurity Scattering to Enhance Thermoelectric Performance in Cr-Doped Ce gamma Co_4Sb_{12}. *Adv. Funct. Mater.* **2015**, *25*, 6660−6670.
(88) Shi, X.; Zhang, W.; Chen, L. D.; Yang, J.; Uher, C. Theoretical study of the filling fraction limits for impurities in $CoSb_3$. *Phys. Rev. B* **2007**, *75*, 235208.
(89) Cutler, M.; Leavy, J. F.; Fitzpatrick, R. L. Electronic Transport in Semimetallic Cerium Sulfide. *Phys. Rev.* **1964**, *133*, A1143−A1152.
(90) Shi, X.; Yang, J.; Wu, L.; Salvador, J. R.; Zhang, C.; Villaire, W. L.; Haddad, D.; Yang, J.; Zhu, Y.; Li, Q. Band Structure Engineering and Thermoelectric Properties of Charge-Compensated Filled Skutterudites. *Sci. Rep.* **2015**, *5*, 14641.
(91) Yang, J.; Xi, L.; Zhang, W.; Chen, L. D.; Yang, J. Electrical Transport Properties of Filled $CoSb_3$ Skutterudites: A Theoretical Study. *J. Electron. Mater.* **2009**, *38*, 1397−1401.
(92) Lee, J.-K.; Choi, S.-M.; Seo, W.-S.; Cheong, D.-I.; Kim, I.-H. Determination of the Thermoelectric Properties in Filled-Skutterudite Systems by Controlling the Process Variables. *Jpn J. Appl. Phys.* **2012**, *51*, 09ML02.
(93) Xiong, Z.; Chen, X.; Huang, X.; Bai, S.; Chen, L. High thermoelectric performance of $Yb_{0.26}Co_4Sb_{12}/y$GaSb nanocomposites originating from scattering electrons of low energy. *Acta Mater.* **2010**, *58*, 3995−4002.
(94) Wang, S.; Yang, J.; Wu, L.; Wei, P.; Yang, J.; Zhang, W.; Grin, Y. Anisotropic Multicenter Bonding and High Thermoelectric Performance in Electron-Poor CdSb. *Chem. Mater.* **2015**, *27*, 1071−1081.
(95) Kim, H.; Kaviany, M.; Thomas, J. C.; Van der Ven, A.; Uher, C.; Huang, B. Structural Order-Disorder Transitions and Phonon Conductivity of Partially Filled Skutterudites. *Phys. Rev. Lett.* **2010**, *105*, 265901.
(96) White, D. P.; Klemens, P. G. Thermal-Conductivity of Thermoelectric $Si_{0.8}Ge_{0.2}$ Alloys. *J. Appl. Phys.* **1992**, *71*, 4258−4263.
(97) Tritt, T. M.; Nolas, G. S.; Slack, G. A.; Ehrlich, A. C.; Gillespie, D. J.; Cohn, J. L. Low-temperature transport properties of the filled and unfilled $IrSb_3$ skutterudite system. *J. Appl. Phys.* **1996**, *79*, 8412−8418.
(98) Yang, J.; Meisner, G. P.; Morelli, D. T.; Uher, C. Iron valence in skutterudites: Transport and magnetic properties of $Co_{1-x}Fe_xSb_3$. *Phys. Rev. B* **2000**, *63*, 014410.
(99) Slack, G. A. Thermal Conductivity of MgO, Al_2O_3, $MgAl_2O_4$, and Fe_3O_4 Crystals from 3° to 300°K. *Phys. Rev.* **1962**, *126*, 427−441.
(100) Nolas, G. S.; Harris, V. G.; Tritt, T. M.; Slack, G. A. Low-temperature transport properties of the mixed-valence semiconductor $Ru_{0.5}Pd_{0.5}Sb_3$. *J. Appl. Phys.* **1996**, *80*, 6304−6308.
(101) Zong, P.-a.; Chen, X.; Zhu, Y.; Liu, Z.; Zeng, Y.; Chen, L. Construction of a 3D-rGO network-wrapping architecture in a $Yb_yCo_4Sb_{12}$/rGO composite for enhancing the thermoelectric performance. *J. Mater. Chem. A* **2015**, *3*, 8643−8649.
(102) Gharleghi, A.; Liu, Y.; Zhou, M.; He, J.; Tritt, T. M.; Liu, C.-J. Enhancing the thermoelectric performance of nanosized $CoSb_3$ via short-range percolation of electrically conductive WTe_2 inclusions. *J. Mater. Chem. A* **2016**, *4*, 13874−13880.
(103) Zhou, X.; Wang, G.; Guo, L.; Chi, H.; Wang, G.; Zhang, Q.; Chen, C.; Thompson, T.; Sakamoto, J.; Dravid, V. P.; Cao, G.; Uher, C. Hierarchically structured TiO_2 for Ba-filled skutterudite with enhanced thermoelectric performance. *J. Mater. Chem. A* **2014**, *2*, 20629−20635.

DOI: 10.1021/acs.chemmater.8b03994
Chem. Mater. 2019, 31, 862−872